Electronic Supplementary Material (ESI) for ChemComm.

Supporting Information for

Bio-inspired Reinforcement of Cyclosiloxane Hybrid Polymer

Yujie Song, Xiuzhi Tang, Yen Nan Liang, Ming Liu, Liying Zhang, Shuguang Bi, Chenzhong Mu, Xiao Hu**

correspondence to:liuming@ntu.edu.sg (Ming Liu) and asxhu@ntu.edu.sg (Xiao Hu)

Materials:2,4,6,8-Tetramethylcyclotetrasiloxane (D4H, Alfa Aesar), 2,4,6,8-Tetramethyl-2,4,6,8-tetravinylcyclotetrasiloxane (D4V, Alfa Aesar), Platinum(0)-1,3-divinyl-1,1,3,3-tetramethyldisiloxane complex (Karstedt's catalyst, 3.2wt% Pt, Alfa Aesar), Allylamine (Alfa Aesar), natural graphite powder LBG8010 (Superior Graphite Company), sulfuric acid (A. R. 95-98 wt%, Sigma-Aldrich), nitric acid (A. R. 67 wt%, Sigma-Aldrich), potassium permanganate (Alfa Aesar), hydrogen peroxide (30%, VMR),and N,N-dimethylformamide (DMF, Sigma-Aldrich) were used as received.

Modification of GO by allylamine: GO was prepared according to a modified Hummer's method and dried in vacuum oven overnight, before modification by allylamine. Dried GO (100 mg) was suspended in DMF (100 ml), and the mixture was probe sonicated for 20 minutes to form a stable suspension. Allylamine (10 ml) was added into GO suspension and the obtained mixture was heated up to 50 ºC for 48 hours under continuous stirring. The solid product was separated by vacuum filtration and washed with sufficient amount of ethanol and DI water to remove DMF and residual allylamine. After dehydration by freeze drying, the fluffy allylamine modified GO (GO-AA) was stored in a desiccator for further use.

Preparation of CHP and CHP nanocomposites: Desired amount of GO or GO-AA was suspended in D_4V by ultrasonic exfoliation. The mixtures were subjected to magnetic stirring to maintain well dispersion. Karstedt's catalyst (0.1 wt%) was added into the mixtures, followed by addition of D_4H (Mass ratio of D_4H:D_4V 1:1). The resultant mixtures were stirred at room temperature until proper viscosity was reached before transferred into Teflon molds and cured at

room temperature in vacuum. After partially cured at 80 ºC for 4 h, the samples (~1 mm thick) were cut into appropriate dimensions and further cured at 150 ºC for 24 h prior characterizations.

Characterizations: Fourier transform-infrared (FTIR) spectroscopy was carried out using a Frontier model with ATR accessory (Perkin Elmer). 16 scans were recorded with resolution of 4 cm-1. Raman Spectrum was recorded by Witec alpha300 SR Confocal Raman Spectroscopy (WITec) with 488 nm wavelength laser and 50 scans were recorded for each sample to ensure the accuracy. X-ray photoelectron spectroscopy (XPS) was carried out on a VG ESCALAB 220I-XL system. The energy calibration was made against the N1s peak and C1s peak during analysis. Optical images were taken in transmission mode using Olympus BX 53 fluorescence microscope. Scanning electron microscopy (SEM) was carried out using FE-SEM 7600F (JEOL). The fracture surfaces were sputter coated with platinum. Transmission electron microscopy (TEM) was carried out using JEM-2010 (JEOL). GO and GO-AA were firstly dispersed in ethanol and then dropped onto a copper grid. For GO-AA/CHP nanocomposites, they were firstly grinded into powder, followed by sonication in ethanol for about 1 week, and the resulting suspension was dropped onto a copper grid. The as prepared TEM samples were dried before loaded into TEM. 3-point bending test was carried out using Tensile Tester Instron 5567 with a 500 N load cell. The sample thickness was about 1 mm and the width was about 10 mm. All the samples were carefully polished before bending tests at a sample span of 32 mm with a 2 mm/min crosshead speed. 4-6 samples were tested for each system. The toughness of CHP and nanocomposites was calculated according to the following equation by measuring the area under the stress-strain curves (Figure S11):

$$T = \frac{\int_0^{\varepsilon_f} \sigma d\varepsilon}{\int_0^{\varepsilon_0} \sigma_0 d\varepsilon}$$

where T is toughness, σ is flexural stress (MPa), ε is flexural strain and ε_f is the final flexural strain (σ_0 and ε_0 stand for flexural stress and final flexural strain of neat CHP).

Modulated Differential Scanning Calorimeter (MDSC) TA 2920 (TA Instruments) was used to test specific heat capacity (C_p). Gas pycnometer Ultrapyc 1200e (QuantachromeCorp) was used to measure the true density of samples in Helium atmosphere. XFA 500 Xenon Flash Apparatus (LINSEIS) was used to get thermal diffusivity of samples at room termpature. In a typical thermal diffusivity test, a round samples with diameter of 0.5 inch and thickness of 2-3 mm was used. Before test, the samples were firstly coated with gold and graphite to get most accurate results. Thermal conductivity was calculated by the following equation:

$$K = \alpha \rho C_p$$

where K is thermal conductivity (Wm-1K-1), α is thermal diffusivity (mm^2s^{-1}), ρ is density of the samples (g cm^{-3}) and C_p is specific heat capacity ($Jg^{-1}K^{-1}$). At least 3 samples were tested for each system to guarantee the reliability of the data.

Determination of sample thickness for 3-pint bending test: Sample thickness for mechanical test and critical thickness were taken into consideration before mechanical tests. Critical thickness of polymer materials is defined as an absolute thickness dimension below which a macroscopically brittle polymer no longer exhibits brittle fracture and instead deforms in a ductile fashion.[1, 2] In order to minimize the effect of thickness, all samples tested were more than 0.5 mm in thickness which is much larger than reported critical thickness (less than 5 micrometer) of silicone resins[3, 4] and thickness of samples were similar for each test.

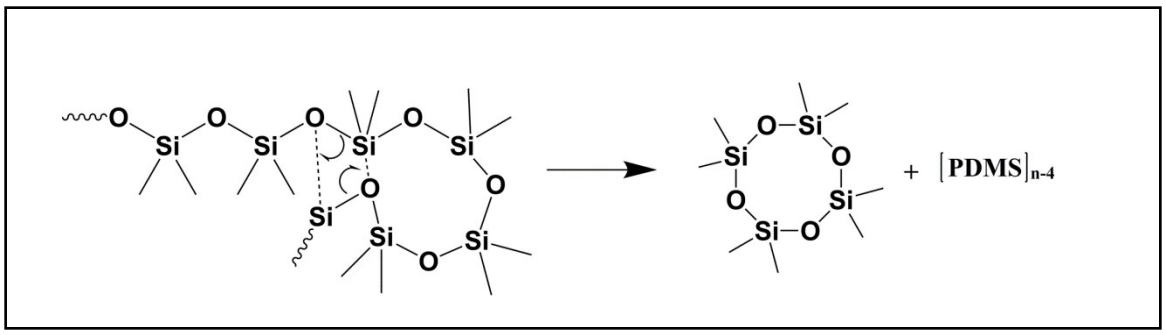

Figure S1. Backbiting decomposition mechanism of PDMS.

During decomposition process, the PDMS chain 'bites back', forming volatile cyclosiloxanes, and shortened PDMS chain. This process keeps cutting PDMS shorter and shorter, leading to fast decomposition at high temperatures.

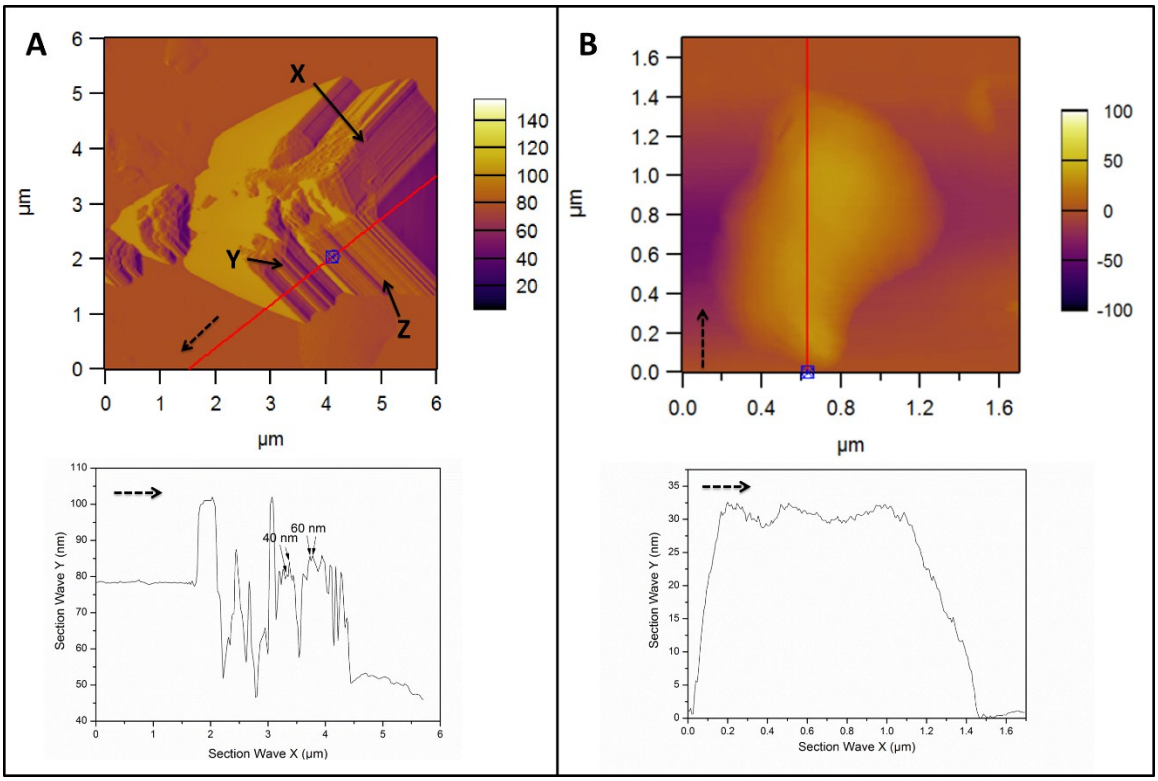

Figure S2. AFM images of (A) powder and (B) exfoliated layer structure of CHP. The dash arrows indicate the directions of section analysis.

The AFM image of powder sample clearly shows that CHP is a layered structure with different orientations. The thickness of each layer is a few tens of nanometers, which correspond to the thickness of exfoliated CHP by sonicating powder sample in ethanol for about 1 week.

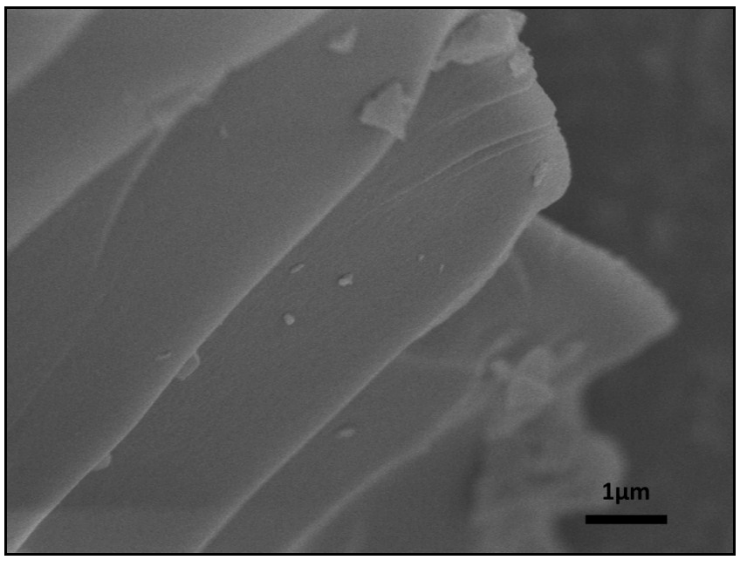

Figure S3. An SEI image of grinded CHP powder.

The powder sample clearly shows that CHP layered structure is a stack of CHP layers.

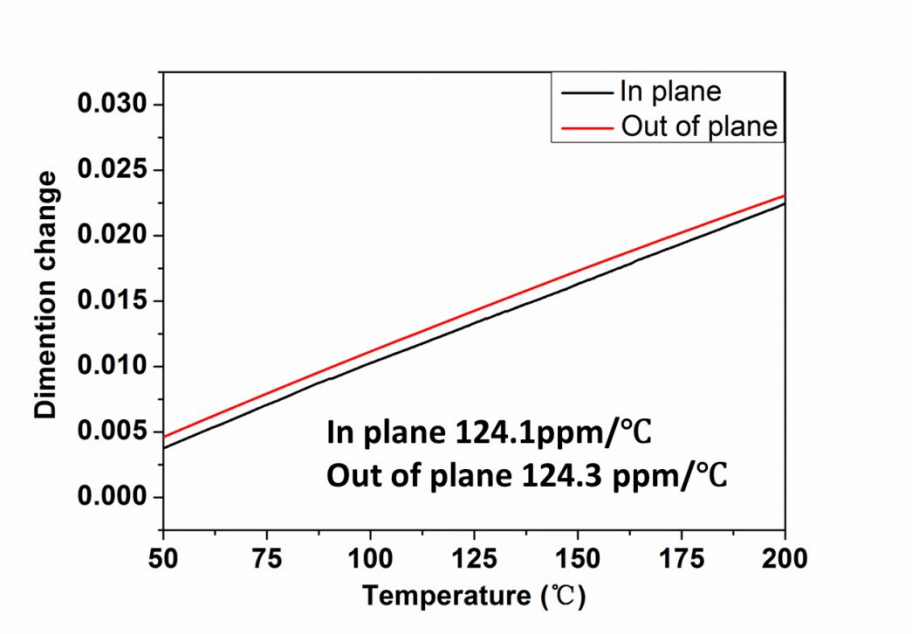

Figure S4. Thermomechanical analysis (TMA) of a piece of flat CHP.

A flat piece of CHP (10mm*10mm*1mm) was used to test the CTEs in different directions. The CTE for 'in plane' is parallel to the surface while the one for 'out of plane' is perpendicular to the surface. The similar CET values along different directions indicated that CHP is isotropic at macro-scale.

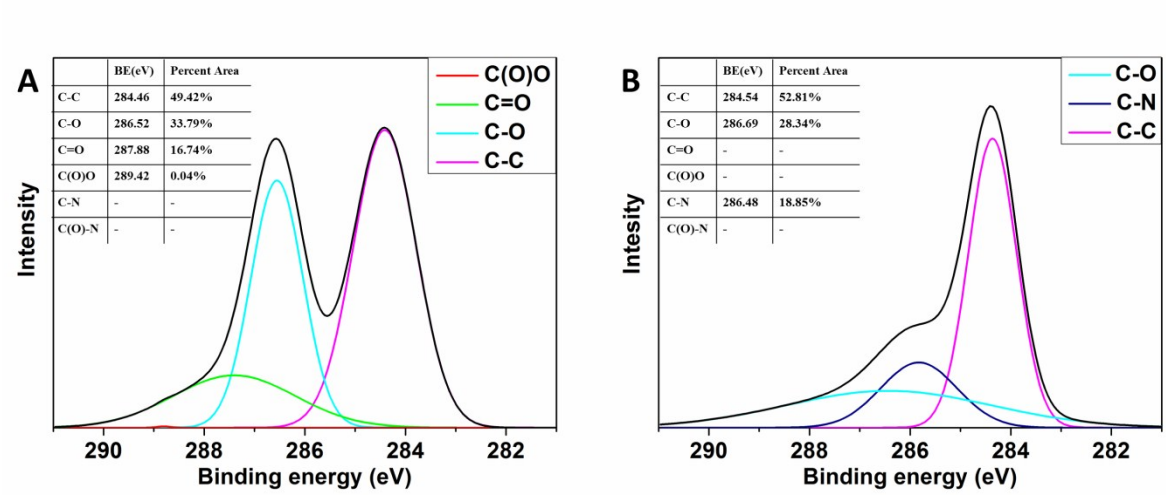

Figure S5. C1s XPS spectra of (A) GO and (B) GO-AA.

C1s XPS peaks were deconvoluted into separate peaks and no peak for C(O)-N (287.43 eV) and C(O)-O (289.42 eV)[5] can be deconvoluted from XPS spectra of GO-AA while C-N peak (286.48 eV) suggests the covalent reaction of epoxide groups and amine groups. As discussed above, carboxyl groups are believed to be distributed on the edge of graphene while epoxide groups are basally decorated. Missing of C=O and C(O)-N signals proved that GO-AA was basally functionalized by allylamine. Another variance between spectra of GO and GO-AA reveals changes in the proportions of oxygen-containing functional groups. The deconvoluted C1s spectrum of GO shows strong C-O signal (286.52 eV) while the one of GO-AA showed decreased intensity. Taking all the points above into consideration, the XPS spectra of GO and GO-AA further proved that modification of graphene nanosheets by allylamine and reduction of GO occur at the same time and the GO-AA is basally functionalized.

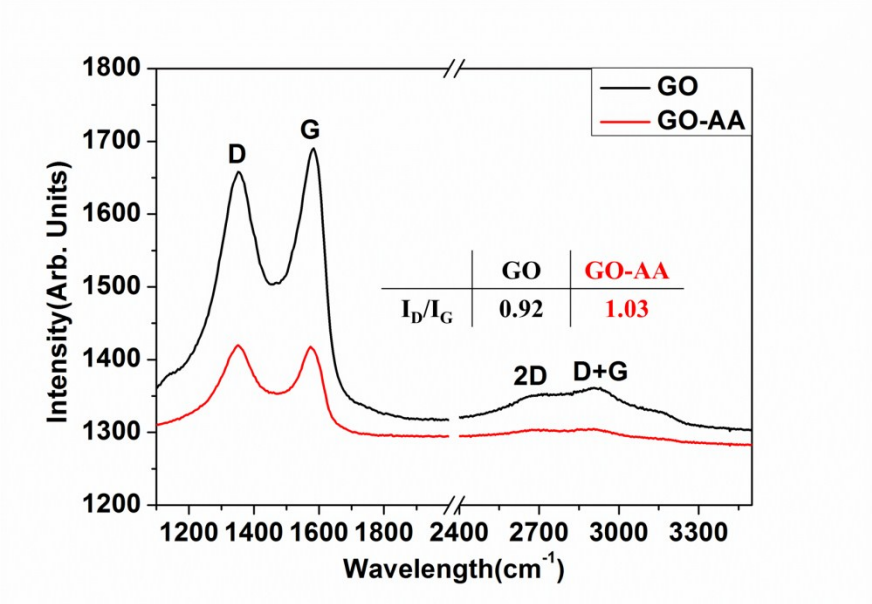

Figure S6. Raman spectra of GO and GO-AA.

The Raman spectrum of GO demonstrate two main peaks at 1354 cm^{-1} and 1581 cm^{-1}, corresponding to D band and G band, respectively. The drastic intensity increased of D and G band in GAC and GAT indicated that the formation of more sp^3 and sp^2 carbon structures. The D band represents the defects of graphene, while the G band is due to the first order scattering of the E_{2g} phonon of the sp^2 carbon atoms of graphene.[6] The G band of GO-AA shifted to 1573 cm^{-1} suggested that GO was successfully reduced by allylamine. The I_D/I_G was increased from 0.92 for GO to 1.03 for GO-AA, indicating the removal of oxygen functional groups and the conversion of sp^3 carbon of GO to sp^2 carbon in the reduced GO. Another difference which should be noticed is 2D bands of GO and GO-AA. 2D bands located at 2718 cm^{-1} are sensitive to layers of graphene.[7, 8] The reduced 2D peak in GO-AA indicated the the success in the exfoliation of the graphene nanosheets.

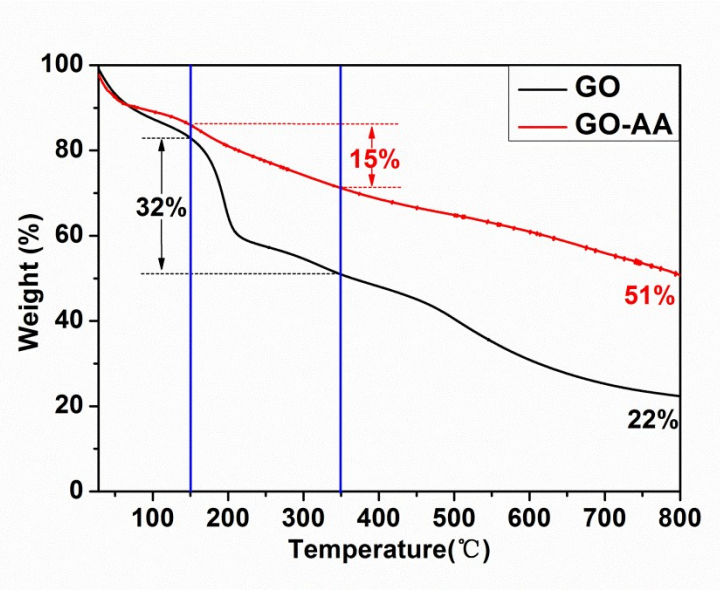

Figure S7. TGA curves of GO and GO-AA in nitrogen.

The poor thermal stability of GO with a low onset thermal degradation around 150 ºC and 32 wt% weight loss between 150 to 350 ºC were due to the cleavage of labile oxygen-containing groups on GO.[9] In contrast, the removal of most of the oxygen-containing groups from GO-AA improved the thermally stablity with only 15 wt% weight loss between 150 to 350 ºC, and the final residual of GO-AA at 800 oC was determined as 51 wt%.

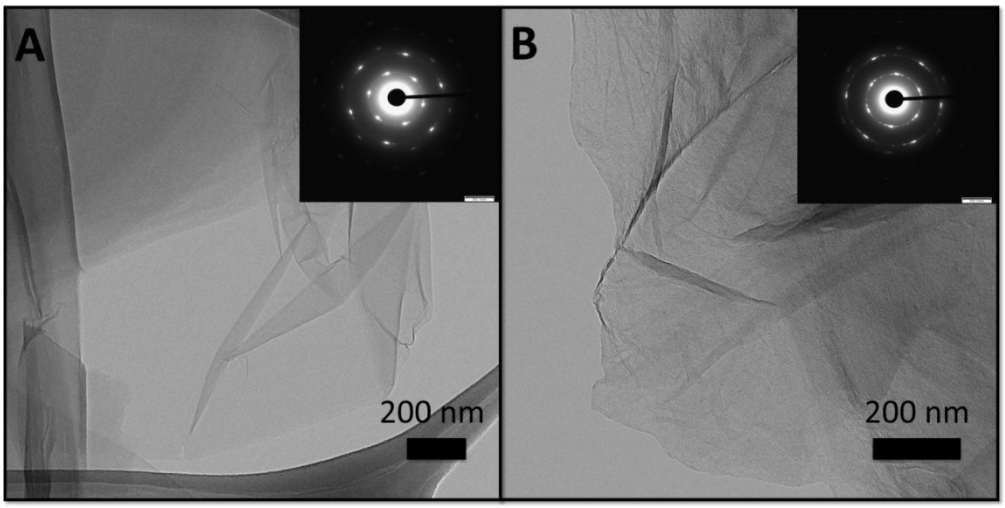

Figure S8. TEM images of (A) GO and (B) GO-AA.

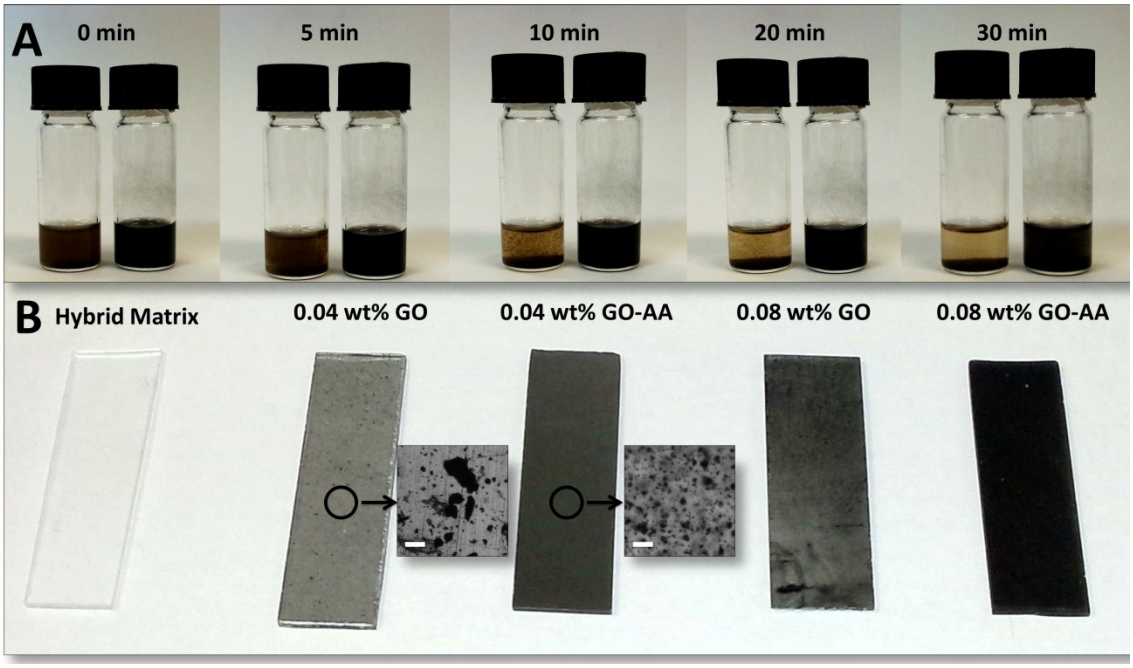

Figure S9. Digital images of (A) GO-D_4V and GO-AA-D_4V suspensions, (B) GO/CHP and GO-AA/ CHP nanocomposites. Inset images are microscope images of corresponding samples, and full microscope images are available in Figure S10.

GO started to aggregate at 5 min and precipitated at 10 min after sonication, while the GO-AA suspension remained stable at 30 min after sonication. Distinct dispersion state of GO and GO-AA in the CHP matrix was clearly visible from the digital images in Figure S9B. Observation of 0.04 wt% nanocomposites by microscope (Inset images of Figure S9B) further proves the improved dispersion of GO-AA in nanocomposite since aggregation of GO can be easily observed while GO-AA were distributed evenly in nanocomposites. The good dispersion of GO-AA inside D_4V was mainly contributed by the decrease in hydrophilicity after modification by allylamine, resulting in improved compatibility of graphene nanosheets with the hydrophobic D_4V monomer, which is an advantage for the solventless process.

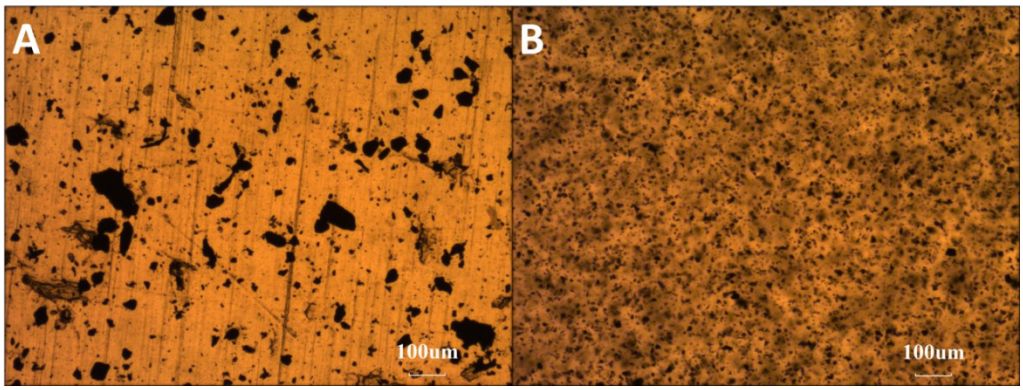

Figure S10. Microscope images of (A) GO/CHP and (B) GO-AA/CHP nanocompoistes with 0.4 wt% loading.

The microscope image of GO nanocomposite clearly showed GO aggregation since large GO particles as large as 100 um can be observed. The microscope image of GO-AA nanocomposite showed evenly dispersed GO-AA nanosheets, which is a result of modification by allylamine.

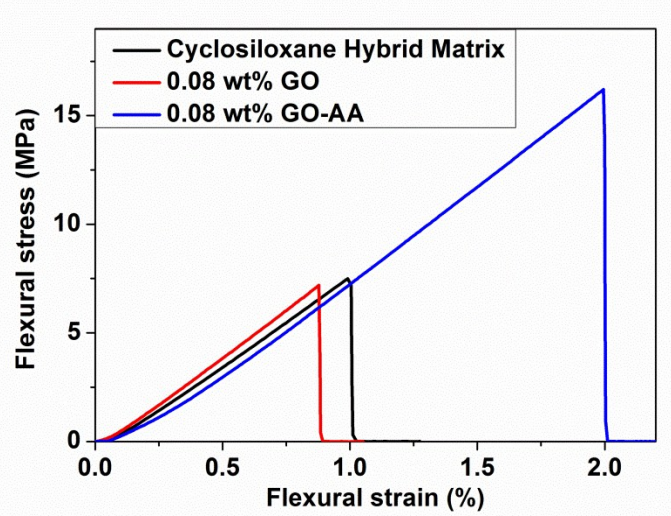

Figure S11. Representative stress-strain curves from 3-point bending test.

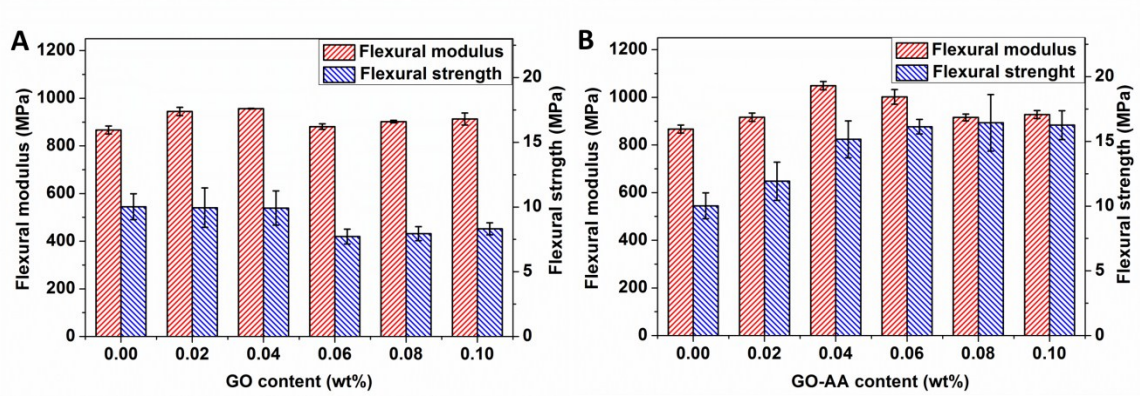

Figure S12. Flexural modulus and flexural strength of (A) GO and (B) GO-AA nanocomposites.

Figure S12 shows that the flexural modulus of GO nanocomposites fluctuates as a function of GO content while the flexural strength decreases with increasing GO-AA content. Compared with GO/CHP nanocomposites, the flexural modulus of GO-AA nanocomposites increased with GO-AA content, maximized at 0.04 wt% before decrease at higher loading. The flexural strength increases with GO-AA content, but less significant when GO-AA loading is lower than 0.04 wt%. The insignificant effect of GO on modulus is due to the weak GO-CHP interfacial interaction resulting from their incompatibility. Together with aggregation of GO nanosheets, these two reasons caused the decrease of flexural strength.[10] For GO-AA/CHP nanocomposites, better dispersion and covalent bonds between GO-AA and the CHP are the two main contributing factors for the increase of flexural modulus before it peaks at 0.04 wt% graphene loading, as well as for the increase of flexural strength with graphene loading from 0.02 wt% to 0.1 wt%. The subsequent decrease of flexural modulus might be due to poor dispersion above weight fraction of 0.04% which reduces the effective area for interaction.[11] Apart from the two main reasons mentioned above, the wrinkled surfaces of GO-AA nanosheets also played an important role in enhancing the mechanical properties of nanocomposites.(See Figure S14 and Figure S15) The wrinkled surfaces of GO-AA nanosheets, together with covalent bonds between graphene nanosheets and CHP,

provide better interfacial interactions. In this case, the ‘double side tape’ GO-AA nanosheets acted as interlocks and load transfers in the CHP matrix, improving the mechanical properties .[12]

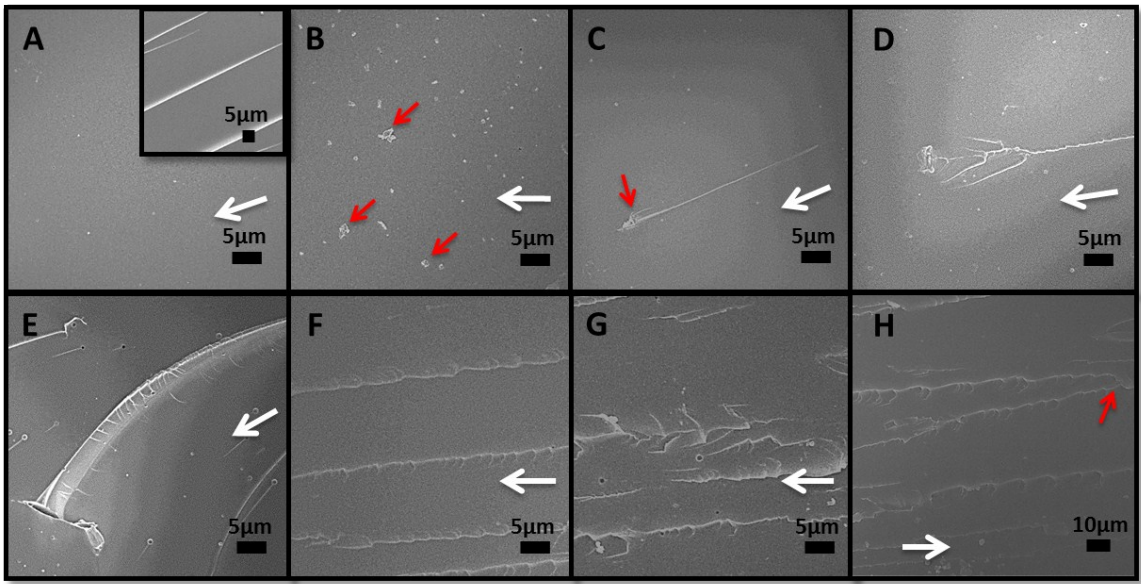

Figure S13. Fracture surfaces of (A) CHP and nanocomposites with (B) 0.04 wt% GO, (C) 0.02 wt% GO-AA, (D) 0.04 wt% GO-AA, (E) 0.06 wt% GO-AA, (F) 0.08 wt% GO-AA, (G) and (H)0.10 wt% GO-AA. Crack propagation directions are indicated by white arrows.

As can be seen from SEM images from fracture surfaces after 3-point bending test, neat CHP displayed a very smooth crack surface (Figure S13A), and occasionally a small number of straight cracks can be observed (Inset image, Figure S13A). The smooth surfaces and straight crack indicated the intrinsic brittle nature of CHP. The fracture surface of 0.04 wt% GO nanocomposite(Figure S13B) was chosen for discussion here, as the representative of all the GO nanocomposites prepared. Smooth fracture surface was observed except some aggregation of GO (Red arrows, Figure S13B). The hydrophilicity of GO and hydrophobicity of CHP caused poor dispersion of GO in D_4V monomer and subsequent aggregation during the curing process, which lead to defects in the CHP matrix. Figure S13C-H show typical fracture surfaces of GO-AA nanocomposites, demonstrating better dispersion without aggregation. Interestingly, different toughening mechanisms were observed at different GO-AA leadings. 0.02 wt% GO-AA

nanocomposite showed a smooth fracture surface (Figure S13C), and only few sites of crack pinning (red arrow, Figure S13C) were observed, in which case the crack front was stoped by GO-AA nanosheet, forming a GO-AA-tail morphology. Crack-pinning can be observed in all GO-AA nanocomposites, but it should be pointed out that crack pinning iis insufficient to achieve satisfactory toughening of the CHP matrix at low graphene loadings (Figure 3C). When GO-AA loading was increased to 0.04%, straight cracks with sub-cracks or microcracks can be observed (Figure S13D). The number of cracks and microcracks grew with GO-AA loading (Figure S13D-G). When the GO-AA loading is 0.08 wt%, the cracks were bamboo-like with many microcracks. The formation of bamboo-like microcracks absorbed the fracture energy, leading to increased toughness. However, when GO-AA loading is 0.10 wt%, the coalescence of microcracks (Red arrow, Figure S13H) resulted in the formation of rougher surfaces, facilitated major crack propagation and reduced the toughness (Figure 3C).

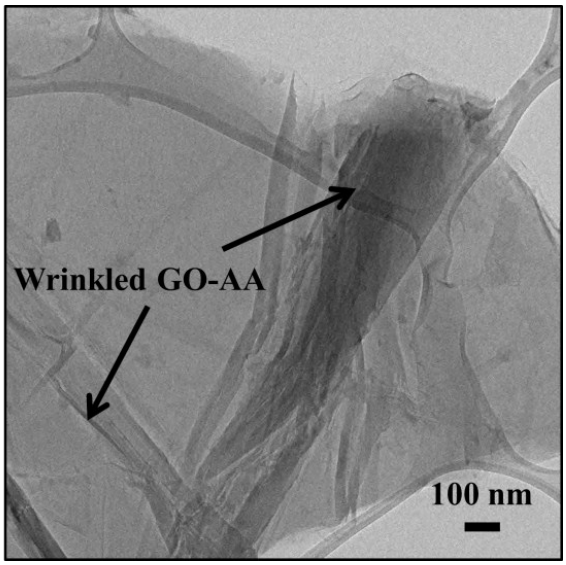

Figure S14. TEM image of wrinkled GO-AA from GO-AA/CHP naocomposites. TEM sample was prepared by exfoliating layered structure with GO-AA via sonicating GO-AA/CHP nanocomposite in ethanol for 1 week.

Figure S14 indicates that GO-AA is wrinkled in CHP matrix, in which case GO-AA nanosheet can provide better interaction between GO-AA and CHP matrix, contributing to enhance mechanical properties.

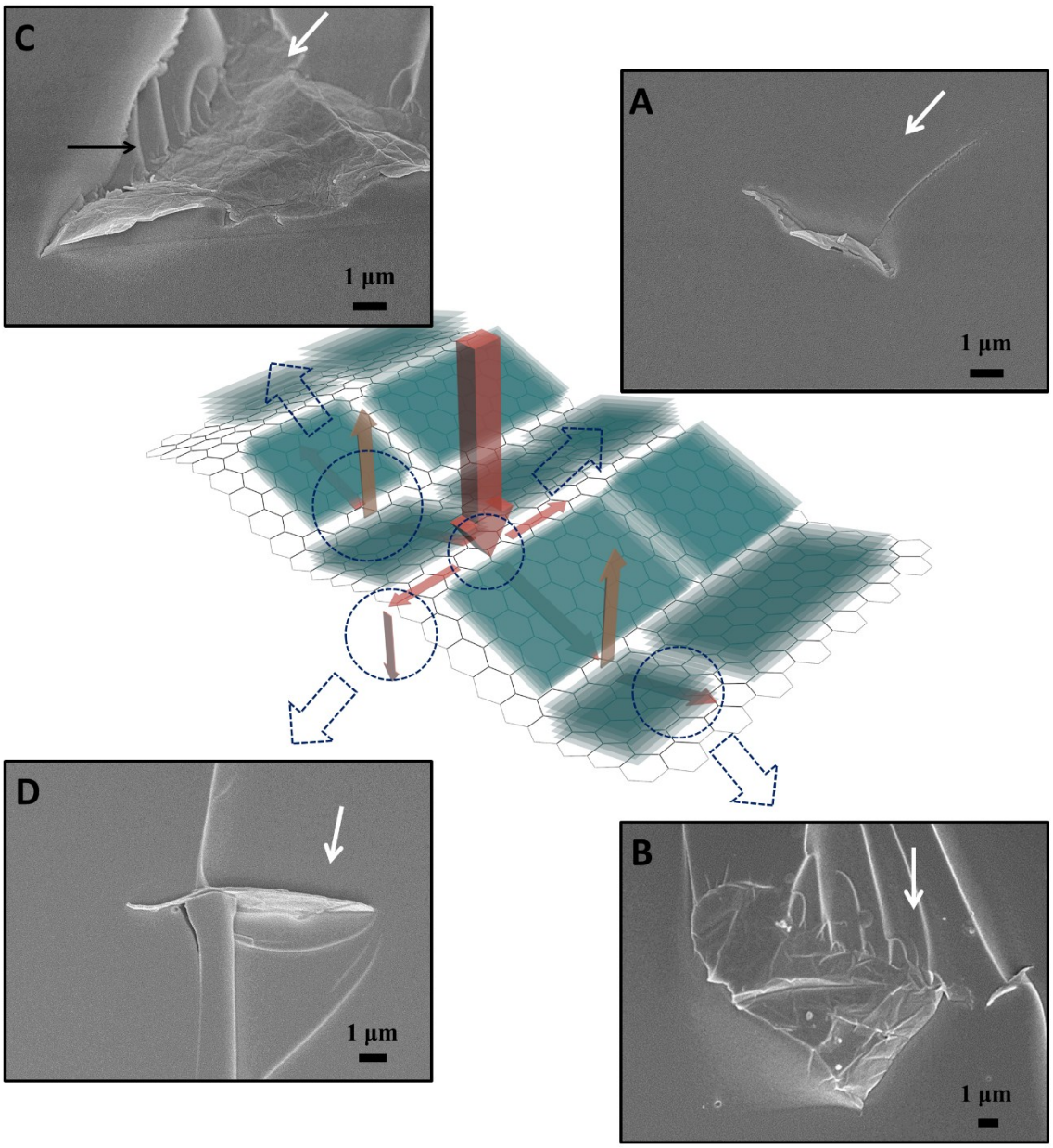

Figure S15. Crack propagation behaviors in GO-AA nanocomposites and formation of (A) crack pinning, (B) graphene trace, (C) graphene trace with microcracks and (D) crack bifurcation. (The colorful arrows indicate the crack propagation. The white arrows in SEI images indicate the crack directions).

Upon encountering a GO-AA nanosheet, the crack will be deflected or tilted along the basal plane directions of GO-AA (Red arrows, Figure S15). If the crack is stopped by GO-AA, crack pinning morphology (Figure S15A) will be observed. Crack pinning was observed in all GO-AA containing CHP nanocomposites, but it cannot be the main mechanism responsible for 156% improvement at only 0.8 wt% loading of GO-AA. In most cases, the deflected or tilted crack continues to propagate along GO-AA surface, leaving graphene trace (Figure S15B). When the deflected or tilted crack along GO-AA surface meets weak boundaries existing between layered structures anchored to surface of 'double side tape' GO-AA, part of the crack will propagate along weak boundaries (orange arrows, Figure S15), forming microcracks (black arrows, Figure S15C) with directions deviated from GO-AA surface. Formation of microcracks allows absorbing more energy during cracking, toughening CHP. Cases are there when part of cracks are pinned, deflected or tilted while the rest continues to propagate, forming bifurcation morphology (Figure S15D). Bifurcation allows crack to change height during propagation[13] and absorb more energy, contributing to toughness of CHP.

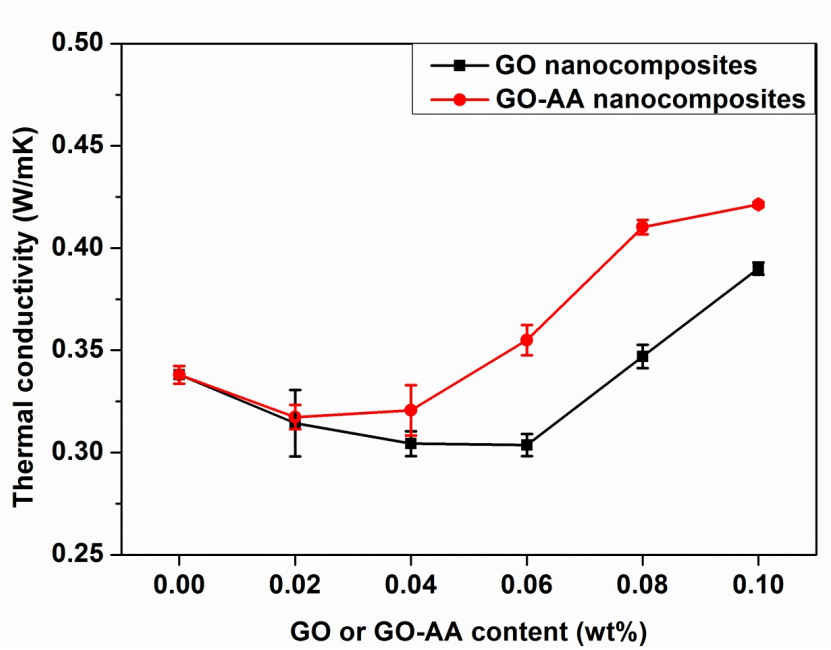

Figure S16. Thermal conductivity of CHP/GO nanocomposites and CHP/GO-AA nanocomposites.

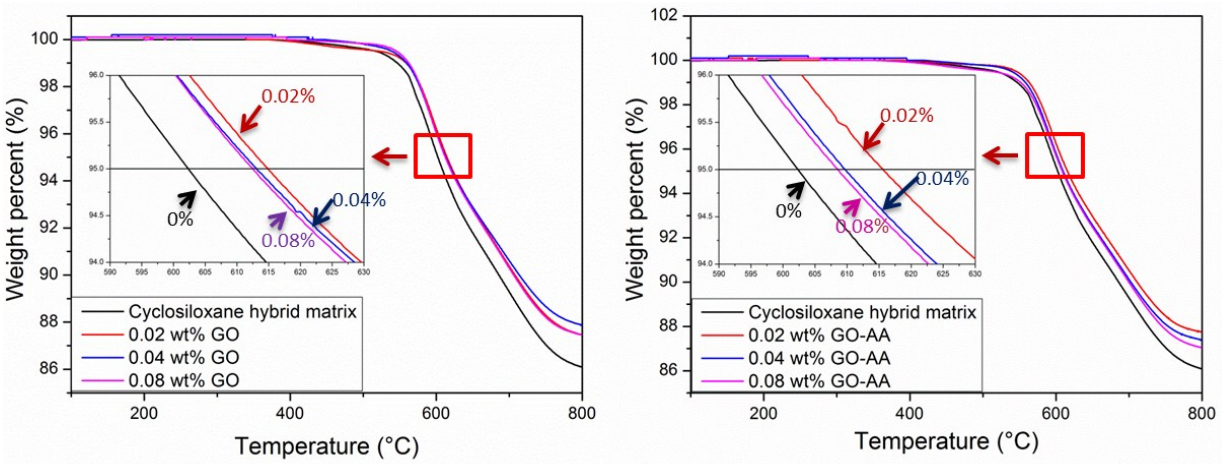

Figure S17. TGA curves of CHP/GO nanocomposites and CHP/GO-AA nanocomposites.

All the samples tested showed better thermal stability than cyclosiloxane polymer matrix. T_{d5} (the temperature where 5% weight loss) and weight retention at 800 °C firstly increased and then decreased with graphene content. The phenomenon can be explained by transfer of phonons, which is necessary for heat conduction in polymers. For low graphene loading, the filler-polymer coupling and filler-filler interfacial coupling are too weak and hinder the transfer of phonons, thus causing increased thermal resistance. However, when graphene loading is higher, the filler-filler interfacial coupling is enhanced since the distance between fillers are smaller, resulting in decrease of the thermal stability[14, 15]. The relatively poorer thermal stability of GO-AA nanocomposites at higher graphene loadings (>0.04 wt%) is due to better dispersion of GO-AA, in which case the filler-filler interfaces coupling is stronger since there is less aggregation of GO-AA.

Table S1. Improvement of thermal conductivity of different matrix-nanofiller systems.

Matrix-Filler	Loading of fillers	Improvement of thermal conductivity/ %	Improvement of thermal conductivity per wt% of fillers/%/wt%	Reference
PDMS-silica coated MWCNT	0.1 wt%	10	100	[16]
Epoxy-MWCNT	0.3 wt%	15.9	53	[17]
Polyurethane- MWCNT	0.5 wt%	26	52	[18]
Polyurethane-functionalized MWCNT	0.5 wt%	47.5	95	[18]
Epoxy- MWCNT	0.5 wt%	25	50	[19]
Epoxy-silica coated MWCNT	0.25 wt%	15.8	63.2	[20]
Epoxy-Graphene	0.1 wt%	7	70	[21]
Polystyrene-graphene	1 wt%	6.8	6.8	[22]
Epoxy- graphene	0.25 wt%	7.9	31.6	[23]
Epoxy- graphene	0.5 wt%	15.8	31.6	[23]
Poly(vinylidene fluoride)-aligned graphene	0.25 wt%	25%	100	[24]
Cyclosiloxane hybrid polymer-functionalized graphene	0.1 wt%	25%	250	This work

REFERENCE

1. M. C. M. van der Sanden, H. E. H. Meijer and P. J. Lemstra, *Polymer*, 1993, **34**, 2148-2154.
2. M. C. M. van der Sanden, H. E. H. Meijer and T. A. Tervoort, *Polymer*, 1993, **34**, 2961-2970.
3. M. Deopura, Ph.D, Massachusetts Institute of Technology, 2005.
4. A. Satorius, Master, Massachusetts Institute of Technology, 2004.
5. X. Wei, L. Mao, R. A. Soler-Crespo, J. T. Paci, J. Huang, S. T. Nguyen and H. D. Espinosa, *Nat. Commun.*, 2015, **6**, 8029.
6. H. Liu, T. Kuila, N. H. Kim, B.-C. Ku and J. H. Lee, *J.Mater. Chem. A*, 2013, **1**, 3739.
7. L. M. Malard, M. A. Pimenta, G. Dresselhaus and M. S. Dresselhaus, *Phys. Rep.*, 2009, **473**, 51-87.
8. A. C. Ferrari and D. M. Basko, *Nat. Nanotechnol.*, 2013, **8**, 235-246.
9. D. R. Dreyer, S. Park, C. W. Bielawski and R. S. Ruoff, *Chem. Soc. rev.*, 2010, **39**, 228-240.
10. Y. T. Park, Y. Qian, C. Chan, T. Suh, M. G. Nejhad, C. W. Macosko and A. Stein, *Adv. Funct. Mater.*, 2015, **25**, 575-585.
11. M. A. Rafiee, J. Rafiee, I. Srivastava, Z. Wang, H. Song, Z. Z. Yu and N. Koratkar, *Small*, 2010, **6**, 179-183.
12. M. A. Rafiee, J. Rafiee, Z. Wang, H. Song, Z.-Z. Yu and N. Koratkar, *ACS Nano*, 2009, **3**, 3884-3890.
13. M. Quaresimin, K. Schulte, M. Zappalorto and S. Chandrasekaran, *Compos. Sci. Technol.*, 2016, **123**, 187-204.
14. J. H. Seol, I. Jo, A. L. Moore, L. Lindsay, Z. H. Aitken, M. T. Pettes, X. Li, Z. Yao, R. Huang, D. Broido, N. Mingo, R. S. Ruoff and L. Shi, *Science*, 2010, **328**, 213-216.
15. K. K. Sadasivuni, D. Ponnamma, S. Thomas and Y. Grohens, *Prog. Polym. Sci.*, 2014, **39**, 749-780.
16. J. Hong, J. Lee, C. K. Hong and S. E. Shim, *J. Therm. Anal. Calorim.*, 2010, **101**, 297-302.
17. C.-H. Kuo and H.-M. Huang, *J. Therm. Anal. Calorim.*, 2010, **103**, 533-542.
18. J.-C. Zhao, F.-P. Du, X.-P. Zhou, W. Cui, X.-M. Wang, H. Zhu, X.-L. Xie and Y.-W. Mai, *Composites Part B*, 2011, **42**, 2111-2116.
19. J. Guo, P. Saha, J. Liang, M. Saha and B. P. Grady, *J. Therm. Anal. Calorim.*, 2013, **113**, 467-474.
20. M.-H. Chung, L.-M. Chen, W.-H. Wang, Y. Lai, P.-F. Yang and H.-P. Lin, *J. Taiwan. Inst. Chem. E*, 2014, **45**, 2813-2819.
21. S. Chatterjee, J. W. Wang, W. S. Kuo, N. H. Tai, C. Salzmann, W. L. Li, R. Hollertz, F. A. Nüesch and B. T. T. Chu, *Chem. Phys. Lett.*, 2012, **531**, 6-10.
22. P. Ding, J. Zhang, N. Song, S. Tang, Y. Liu and L. Shi, *Compos. Sci. Technol.*, 2015, **109**, 25-31.
23. A. Li, C. Zhang and Y.-F. Zhang, *J. Appl. Polym. Sci.*, 2017, **134**.
24. H. Guo, X. Li, B. Li, J. Wang and S. Wang, *Mater. Design*, 2017, **114**, 355-363.